Ionomer Content Optimization in Nickel-iron-based Anodes with and without Ceria for Anion Exchange Membrane Water Electrolysis

Emily Cossar[a], Alejandro O. Barnett[b,c], Frode Seland[d], Reza Safari[e], Gianluigi A. Botton[e], Elena A. Baranova[a*]

[a] *Department of Chemical and Biological Engineering, Centre for Catalysis Research and Innovation (CCRI) University of Ottawa,161 Louis-Pasteur Ottawa, Canada, K1N 6N5*

[b] *SINTEF Industry, Sustainable Energy Technology Department, New Energy Solutions Group, Trondheim, Norway*

[c] *Department of Energy and Process Engineering, Norwegian University of Science and Technology, NO-7491 Trondheim, Norway*

[d] *Department of Materials Science and Engineering, Norwegian University of Science and Technology, NO-7491 Trondheim, Norway*

[e] *Department of Materials Science Engineering, McMaster University, 1280 Main St. W., Hamilton, Ontario, Canada L8S 4L8*

***Corresponding author email:** elena.baranova@uottawa.ca

***Corresponding author number:** 613-562-5800 ext. 6302

Hydrogen production from anion exchange membrane water electrolysis (AEMWE) is an efficient cost-effective solution to renewable energy storage. Contrary to proton exchange membrane (PEM) electrolysis, AEMWE requires further optimization of its cell design, particularly for the kinetically unfavourable oxygen evolution anode half-cell reaction (OER). In this work we optimize the commercial Fumatech fumion ionomer content in AEMWE anodes using nickel (Ni) nanoparticles (NP) synthesized by chemical reduction. The optimal ionomer content is then applied to Ni-iron (Fe)-based NPs with and without ceria (CeO_2), all prepared using the same method. Scanning Electron Microscopy (SEM) of the resulting electrode surfaces, Particle-size Distribution (PSD) of the catalyst inks, and in-situ testing of the monometallic Ni NPs show that the best and most active catalytic layer is obtained using 15 wt% ionomer. AEMWE performance and short-term durability are evaluated in different concentrations of potassium hydroxide (KOH), where the $Ni_{90}Fe_{10}$ is the best performing Ni-based electrode showing 1.72 V at 0.8 A cm^{-2} in 1 M

KOH after IR-correction, and a degradation rate of 3.3 mV h^{-1}. The addition of ceria to the Ni-based catalysts shows more consistent mass transfer over time likely due to more efficient water transport and bubble release.

Key Words

nickel, iron, ceria, oxygen evolution reaction, anion exchange membrane water electrolysis, ionomer optimization

1. Introduction

The production of hydrogen via anion exchange membrane water electrolysis (AEMWE) is an economically feasible method for renewable energy storage, which can be easily integrated into a sustainable hydrogen-based energy system[1–4]. The advantages of AEMWE are well known[1,3,13,5–12]. One of the main advantages of this design comes from the use of a anion exchange membrane (AEM), which allows for a compact, low resistance cell design[5,9,10,14]. The AEM conducts hydroxide ions, while efficiently separating oxygen and hydrogen, allowing for higher operating current densities in comparison to traditional alkaline electrolyzers, which employ porous diaphragms as separators[15,16]. Additionally, contrary to its proton exchange membrane (PEM) equivalent, AEMWE systems allow the use of inexpensive non-noble metals as electrode materials due to their high stability and corrosion resistance in an alkaline environment[15,17–21]. Particularly, nickel-based catalysts have been well investigated as both anodes and cathodes in alkaline electrolysis systems[22–27]. The anode of the alkaline electrolyser is responsible for the oxygen evolution reaction (OER), a kinetically unfavourable reaction due to multiple electron transfer steps[22,28], while the cathode is responsible for the hydrogen evolution reaction (HER).

In an AEMWE system, one of the most important parts of the membrane electrode assembly (MEA) is adding the right amount of ionomer to the catalytic layers. In AEMWE, anion exchange ionomers (AEI) are used. AEIs are anion-conducting polymer electrolytes, consisting of positively charged functional groups bound to a polymer backbone[29]. In a catalytic layer, AEIs are used to form a porous network, which facilitates ion transport to the reaction sites as well as gas permeability, while also serving as a binder for the catalyst particles[30–32]. The amount of ionomer must be optimized because there are consequences to having too little or too much it.

Many studies[30–36] show that having too little ionomer in the catalytic layer results in poor adhesion of the catalytic layer and low ion transport and gas permeability through the layer. On the other hand, having too much ionomer can cause particle agglomeration that can block catalyst sites as well as inhibit mass transport through the catalytic layer. Ionomers may also adsorb onto catalytic sites, reducing the active area available[37]. Having too much ionomer with readily access to water may cause the catalytic layer to lose its structural integrity due to dissolution of the ionomer into the electrolyte[31].

There are a few studies that cover ionomer optimization in AEMWE anodes. Vincent *et al.* [31] tested ionomer amounts in their electrolyser anode ranging from ~9-33% in their 5 cm^2 active area cell. They used a CuCoOx (Acta 3030®) and a Ni/(CeO_2-La_2O_3)/C) (Acta 4030®) catalyst for their OER and HER catalysts, respectively, set up in the CCS format. The loadings of the OER and HER catalysts on the porous carbon substrates were 30 and 7.4 mg cm^{-2}, respectively. The membrane used was the Tokuyama A-201 which was paired with the Acta I_2 alkaline ionomer. In their study, they found that increasing the ionomer content caused voltage drops in the cell, which were much more significant at ionomer concentrations higher than 20%. Ionomer contents lower than 9% caused large cracks in their catalyst layer, therefore the optimal ionomer content was found to be 9%. This ionomer loading resulted in a system performing at 0.5 A cm^{-2} at 1.95 V using 1% potassium carbonate at 60°C as the electrolyte.

Park *et al.* [32] tested ionomer contents of 10, 20 and 30 wt% in their 5 cm^2 active area cell. They used a catalyst coated membrane (CCM) MEA configuration with IrO_2 and 40 wt% Pt/C as OER and HER catalyst, respectively. In this work their anode loading was optimized to 4 mg cm^{-2} and the cathode was set to 0.4 mg cm^{-2}. Their cell was run with 1 M KOH at 70°C. The membrane used in their study was the Fumatech FAA-3-50, which was paired with the Fumatech

FAA-3-Br anionic ionomer. In their study, Park *et al.* [32] found that the 20 wt% ionomer showed the best performance and the lowest charge transfer and cell resistance. They concluded that 20 wt% was the optimal amount when considering the trade-off between available active sites and pore morphology. The optimal performance found was 1.15 A cm^{-2} at 1.8 V at 70°C.

Cho *et al.* [33,34] tested ionomer amounts varying from 5 to 20 wt% in the anode catalytic layer in their 2.5x2.5 cm^2 active area cell in two separate works. Their OER and HER catalysts were IrO_2 and 46.5 wt % Pt/C, respectively, assembled using the CCS method. The system operated at 50°C. The membrane used was the Tokuyama A-201, while the ionomer was a 60 wt% polytetrafluoroethylene (PTFE) dispersion in water. In their first study[33], the optimal ionomer content was found to be 9 wt% showing a performance of 0.299 A cm^{-2} at 1.8 V for an anode feed supply of 0.5 M potassium hydroxide (KOH) and a cathode feed of deionized water. 9 wt% ionomer allowed for a balance between covered active sites and secondary pore formation. In the second study[34], 20 wt% ionomer content showed the best result achieving a current of 1.07 A cm^{-2} at 1.8 V for 0.5 M KOH at the anode and a dry cathode. The higher ionomer content was needed to avoid catalyst detachment and maintain long-term performance. It is interesting to note here that simply changing the electrolyte feed conditions changed the optimal ionomer content, implying that every set of operating parameters and conditions must have its own ionomer optimization step.

In our previous work[26], we performed a preliminary evaluation of Ni-based nanoparticles (NPs) as oxygen evolution catalysts in AEMWEs. Small amounts of iron were added to the Ni NPs to enhance oxygen evolution activity as Fe is a well known OER promoter for Ni catalysts[18,20,22,38–43]. Ceria was also tested as a support to the NPs to further promote catalytic activity due to ceria's good electronic and ionic conductivity as well as its oxygen storage

and release properties[28,38,39,44,45]. The results of this work were promising, showing overall cell voltages between 1.85 and 1.90 V in 1 M KOH at 50°C. The ionomer content used in the anode layers of this work was however simply set to the amount already optimized for the Ir black benchmark. Since this study as performed, we have completed an extensive ex-situ OER evaluation of multiple iron and ceria amounts in the Ni-based catalysts, showing that the best performing OER catalysts include $Ni_{90}Fe_{10}$ and $Ni_{80}Fe_{20}$, both with and without 10 wt% CeO_2[46]. As such, the goal of this study was to investigate the effects of the Fumatech fumion FAA-3-SOLUT-10 commercial ionomer content in the Ni-based anode layer of a single cell electrolyser and find the required optimal ionomer content. Ink properties such as particle size distribution measurements using different ionomer contents with Ni NP electrocatalysts are reported, and the catalytic layer morphology, mechanical stability, and electrochemical performance of the resulting electrodes are evaluated to narrow in on the optimum amount of ionomer. Finally, $Ni_{90}Fe_{10}$ and $Ni_{80}Fe_{20}$ catalysts with optimized ionomer content, both with and without the addition of 10 wt% CeO_2, are evaluated as anodes in an AEMWE single cell.

2. Materials and Methods

2.1. Material Synthesis

The Ni-based nanoparticles were synthesized by chemical reduction in ethanol using sodium borohydride as described in detail in our previous work [26]. To summarize the method to make Ni NPs, a nickel chloride hexahydrate precursor salt ($NiCl_2 \cdot 6H_2O$, 99.999%, Sigma Aldrich, St. Louis, MO, USA) is dissolved in ethanol (EtOH, 99%, Greenfield, Grayslake, IL, USA) by magnetic stirring, then chemically reduced using sodium borohydride ($NaBH_4$, ≥98%, ACROS, Geel, Belgium). The NPs are then removed from the dispersion and washed 3x in EtOH using a centrifuge run at 6000 rpm for 10 minutes (mins) per wash. Once the materials are washed, they

are freeze-dried over night to remove the remaining EtOH. To add iron or ceria to the Ni NPs, iron sulphate heptahydrate ($FeSO_4 \cdot 7H_2O$, ≥99%, Sigma Aldrich, St. Louis, MO, USA) and cerium oxide nanopowder (CeO_2, 99.5%, Alfa Aesar, Haverhill, MA, USA) are dissolve in EtOH in separate flasks. Once dissolved, the Ni, Fe and CeO_2 solutions are mixed and chemically reduced together. The prepared samples of this study include Ni, $Ni_{90}Fe_{10}$ (at%), $Ni_{80}Fe_{20}$ (at%), as well as $Ni_{90}Fe_{10}$/10 wt% CeO_2 and $Ni_{80}Fe_{20}$/10wt% CeO_2.. It is important to note that at a small quantity of 10 wt%, CeO_2 is likely present as a catalyst promoter, rather than a catalyst support. All glassware was cleaned using the Aqua Regia procedure of a volumetric 2:1 ratio of hydrochloric acid to nitric acid (HCl 37%, HNO_3 70%, Sigma Aldrich, St. Louis, MO, USA).

2.2. Material Characterization

The transmission electron microscopy (TEM) images of the $Ni_{90}Fe_{10}$, $Ni_{80}Fe_{10}$ and $Ni_{90}Fe_{10}$/10 wt% CeO_2 nanoparticles were taken using the Philips CM12 operating at 120 kV. The TEM images of the $Ni_{80}Fe_{20}$/10 wt% CeO_2 NPs were taken on the JEOL JEM 2010 Field Emission Transmission Electron Microscope (FETEM) (Tokyo, Japan) with an operating voltage of 200 kV. For characterization of the monometallic Ni particles, see our previous work [26]. The Brunauer-Emmett-Teller (BET) specific surface areas of the nanoparticles as well as the Barrett-Joyner-Halender (BJH) pore size distributions were evaluated using the Micrometrics 3Flex Version 5.00 analyser. Once the samples were degassed under nitrogen flow at 110°C, the measurements were taken by holding 30°C for 10 mins, 75°C for 15 h and 25°C for 4 h. The temperature ramp for all transitions was 10°C/min. Particle-size distribution (PSD) measurements of the catalyst inks were carried out using the Horiba Partica LA-960 (Kyoto, Japan) PSD analyzer. Measurements were taken under no sonication, as well as with 30 s and 180 s (3 minutes) of sonication. Finally, the

catalyst coated surfaces were analyzed under the Hitachi SU6600 (Hitachi High-Tech, Krefeld, Germany) field emission gun scanning electron microscope (FEG SEM) at 20 kV.

2.3. In-situ Experiments

2.3.1. AEMWE Setup

2.3.1.1 Cell and System Configuration

The in-situ AEMWE measurements were carried out in a modified 25 cm^2 parallel flow field fuel cell hardware (balticFuelCells Gmbh, Schwerin, Germany). In comparison to our previous study[26], the increased active area here is used to put our catalysts to the test in a more representatively sized electrolyser, accounting for active area dependant activity. While this area is not comparable to testing in an stack, like in the work of Kim *et al.*[27], where they performed electrolysis testing on a stack of 26 unit cells having an active area of 200 cm^2, it is still on the larger side of the active areas reported in literature, which range from around 1 - 28 cm^2[5,18,31,33,47–52], with most studies conducted with an area under 10 cm^2. Aside from the cell, the electrolyser setup included a 5 L Teflon electrolyte tank and a double headed peristaltic pump, which was used to pump 300 mL min^{-1} of potassium hydroxide (KOH, ≥85%, Sigma Aldrich, St. Louis, MO, USA) electrolyte around the anode and cathode sides of the system. The KOH electrolyte was made using Milli-Q® water (H_2O, Milli-Q® Millipore, 18.2 MΩ cm et 293 K). To heat and control the system temperature to 50 ± 2°C for all experiments, the electrolyser cell as well as both sides of the KOH tank were equipped with heating elements and temperature sensors. The membrane used for all experiments was a commercial anion exchange membrane (fumasep FAA-3PE-30, Fumatech, Bietigheim-Bissingen, Germany). This membrane was paired with a 10 wt% solution of a commercial anionic ionomer (fumion FAA-3-SOLUT-10, Fumatech, Bietigheim-Bissingen, Germany). To secure the membrane and help seal the cell, the membrane

was sandwiched between two gaskets (0.35 and 0.5 mm thick, 35 FC-PO 100 Ice Cube Sealing, Quintech, Göppingen, Germany). For a schematic of the electrolyser cell, see Figure S1.

2.3.1.2 Ni-based Electrodes

To formulate the Ni-based anode inks, the NPs were first measured out then mixed with Milli-Q® water and the ionomer. Once the ionomer was added, the dispersion was sonicated in an ultrasonic bath (45 Hz Ultrasonic Cleaner USC300TH, VWR International, Radnor, PA, USA) for 5 mins over ice. Next, isopropanol (IPA, 99.9%, Fischer Scientific, Hampton, NH, USA) was added at a 50:50 ratio of water to IPA. The %solids in the ink was 3 for optimal spraying. Once all the ink components were mixed, the ink was sonicated in an ultrasonic bath (45 Hz) for 10 mins over ice and then further mixed using an ultrasonic probe at 40% amplitude for 5 minutes, 5 s on/off (20 kHz Branson 450 Digital Sonifier, Marshall Scientific, Hampton, NH, USA) over ice. Ionomer nominal loadings of 7, 15, 25, 35 and 45 wt% in the resulting electrodes were made.

All electrolysis experiments were carried out using the catalyst coated substrate (CCS) method. When optimizing the ionomer content using the monometallic Ni NPs, the anode layer ink was hand sprayed onto a carbon fibre paper (Toray Paper 090, FuelCellStore, Texas, USA) to a final loading of 5 mg cm^{-2} (metallic weight) using an air brush (Cocraft airbrush sprayer, 0.35 mm mouthpiece). As using a carbon paper on the anode side significantly increased the initial cell resistance, a cell activation procedure was performed (keeping the cell current at 0.5 A cm^{-2} until the potential stabilized) to hydrate the carbon paper prior to polarization curve measurements. For the electrolysis experiments using the optimized ionomer in the catalytic layers, the $Ni_{90}Fe_{10}$ and $Ni_{80}Fe_{20}$ with and without CeO_2 catalysts were sprayed onto a 1 mm thick gold coated titanium porous transport layer (PTL, Ti felt, Bekaert, Zwevegem, Belgium) instead of the carbon paper.

It should be noted that the actual metal loadings obtained differ slightly from the desired amount of 5 mg cm^{-2} due to slight variations in the amount of waste generated during electrode preparation. For the actual catalyst loadings, see Table S1 in the Supplementary Information (SI). Additionally, AEMWE testing was performed on the $Ni_{90}Fe_{10}$ electrode with less sonication prior to electrode spraying to observe whether sonication time impacted AEMWE performance. This is shown in Figure S2, S3 and Table S2, with a summary of tested EIS models found in Table S3. While the effects of ink sonication could not be properly analyzed here, the results do show that sonicating the ink for longer helps more efficiently air brush the electrode, which results in a higher electrode loading and therefore better AEMWE performance. For more information on this short study, see the SI.

2.3.1.3 Benchmark Electrodes

Commercial iridium black (Alfa Aesar, Haverhill, MA, USA) was used as a performance benchmark with an anode loading of 3 mg cm^{-2} hand sprayed on a gold coated Ti felt PTL. As for the cathode layer, commercial platinum supported on carbon (Pt/C, 60 wt% metal on support, Alfa Aesar, Haverhill, MA, USA) was used at a loading of 1 mg cm^{-2} hand sprayed onto a carbon paper PTL. To properly study the different electrolysis anodes, the cathode layer was identical for all experiments. The benchmark electrode inks were prepared similarly to the Ni-based ones, however the %solids was set to 2 and the first step in the sonication sequence was done for 15 mins instead of 5. Furthermore, the resulting ionomer content in the electrode layers was 7 and 23 wt% for the Ir black benchmark anode and the Pt/C cathode, respectively.

2.3.2. AEMWE Performance Evaluation

2.3.2.1 Ionomer Optimization

To optimize the ionomer content in the monometallic Ni electrodes, the best three anodes in terms of mechanical stability, were tested in the electrolyser. The electrodes with 7, 15 and 25 wt% ionomer were chosen. The in-situ performance evaluation consisted of polarization experiments carried out using a BioLogic high current potentiostat/galvanostat (HCP-803, BioLogic Science Instruments, Seyssinet-Pariset, France) that was operated using a custom-made LabVIEW program. The polarization curves were carried out by stepping from 0 to 50 A (0 to 2 A cm^{-2}). To avoid equipment damage and maintain safe cell operation, the program was manually stopped when the measured voltage surpassed 2 V. Next, electrochemical impedance spectroscopy (EIS) measurements were carried out with the HCP-803 using the EC-Lab® software. EIS spectra were measured at a fixed direct current (DC) supply of 1, 5 and 18 A (0.04, 0.2 and 0.72 A cm^{-2}) with an alternating current (AC) supply of ± 5%DC, over a frequency range of 50 kHz down to 200 mHz. The current spectra obtained at 5 A are reported in this article. All experiments were carried out at 50 ± 2°C in 1 M KOH.

2.3.2.2 Ni-based Material Evaluation

Once the ionomer was optimized to 15 wt%, the performance of the $Ni_{90}Fe_{10}$, $Ni_{80}Fe_{20}$, $Ni_{90}Fe_{10}$/10 wt% CeO_2 and $Ni_{80}Fe_{20}$/10 wt% CeO_2 materials was evaluated. This was done by performing the experiments described in Section 2.3.2.1 in 1 M and 0.1 M KOH. When switching electrolytes, the system was washed by cycling 5 L of Milli-Q® water for 15 minutes. An identical experimental sequence was also performed using the Ir black benchmark anode. In addition to performing polarization and EIS measurements in both 1 M and 0.1 M KOH, preliminary electrode stability testing was carried out by fixing the cell current at 12.5 A (0.5 A cm^{-2}) for 12 hours. To

observe any changes in cell resistances over time, EIS measurements were done at a DC of 12.5 A (0.5 A cm^{-2}) with an AC of ± 5%DC over a frequency range of 50 kHz down to 200 mHz after every hour during this constant current polarization.

3. Results and Discussion

3.1. Material Characterization

3.1.1. Nanoparticles

Figure 1 shows TEM images for $Ni_{90}Fe_{10}$ (Figure 1a), $Ni_{80}Fe_{20}$ (Figure 1b), $Ni_{90}Fe_{10}$/10 wt% CeO_2 (Figure 1c) and $Ni_{80}Fe_{20}$/10 wt% CeO_2 (Figure 1d). Overall, the NiFe particles are very small in size (estimated as 4-6 nm), however they are difficult to see because when taking TEM images, the particles agglomerate under the electron beam. While it can be hard to identify individual particles on the TEM images, in our previous work[26], we ran X-ray diffraction (XRD) on the particles, which shows broad diffraction peaks, which confirms the presence of nanostructures with nanocrystallites. In comparison to the $Ni_{90}Fe_{10}$ particles, the $Ni_{80}Fe_{20}$ particles show an additional flake-like phase. This flake-like phase could be due to the increased iron content or residues of the reactants or incomplete washing. As for the CeO_2-containing materials, both samples show that ceria is not well blended with the metallic content resulting in somewhat inhomogeneous samples. This can, however, be expected due to the large size of CeO_2 (15 - 30 nm) in comparison to the small nanoparticles, as well as the relatively small specific surface area of ceria (30 – 50 m^2 g^{-1}). More information on the characterization of these materials can be found in our other works[26,46].

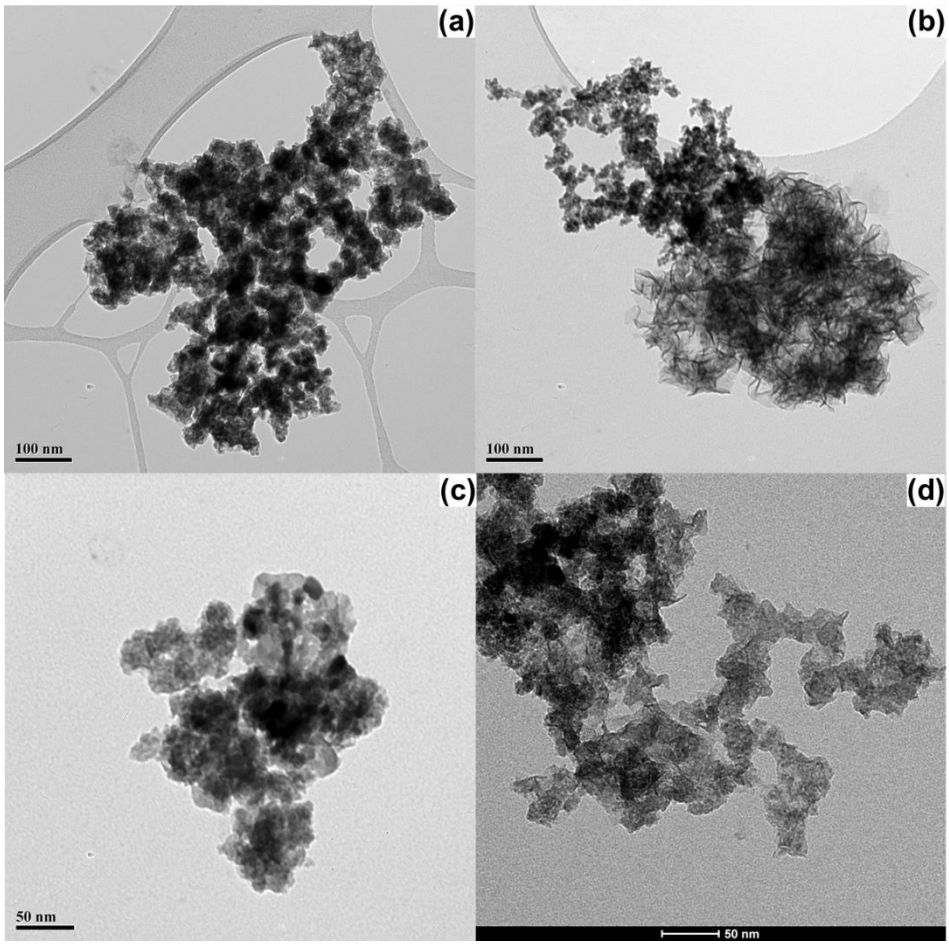

Figure 1: TEM image of (a) $Ni_{90}Fe_{10}$, (b) $Ni_{80}Fe_{20}$, (c) $Ni_{90}Fe_{10}$ / 10 wt% CeO_2 and (d) $Ni_{80}Fe_{20}$ / 10 wt% CeO_2 nanoparticles.

Figure S4 in the SI shows the BJH adsorption pore size distribution by incremental volume (Figure S4a) and by incremental area (Figure S4b). Table 1 summarizes the key information for the BET and BJH analysis.

Table 1: Summary of BET and BJH analysis.

Material	**BET area [$m^2 g^{-1}$]**	**Ads pore D_{ave} [Å]**
Ni	91.16	122.64
$Ni_{90}Fe_{10}$	53.68	179.19
$Ni_{80}Fe_{20}$	158.10	94.21
$Ni_{90}Fe_{10}$/10 wt% CeO_2	112.74	138.36
$Ni_{80}Fe_{20}$/10 wt% CeO_2	220.76	91.62

The $Ni_{90}Fe_{10}$ particles show the smallest BET surface area of 53.68 $m^2 g^{-1}$. Overall, adding ceria increases the BET surface area of the sample, however, this increase is likely attributed to the presence of large ceria particles in the samples (15 – 30 nm with a specific surface area of 30 – 50 $m^2 g^{-1}$). While we have observed in our previous work[46] that ceria agglomerates separately from Ni and Fe, it is also possible that some NiFe NPs are dispersed on ceria, resulting in a higher specific area. As for the adsorption pore size, there is somewhat of an opposite trend. The $Ni_{90}Fe_{10}$ material has the largest pores, and the ceria containing materials show smaller pore sizes than their metallic equivalent.

3.1.2. Ni Catalyst Inks

Figure 2 shows the effect of ionomer content on the particle-size distribution measured for monometallic Ni catalyst inks containing 7, 15, 25, 35 and 45 wt% of the ionomer. The measurements were taken after 180 s of sonication.

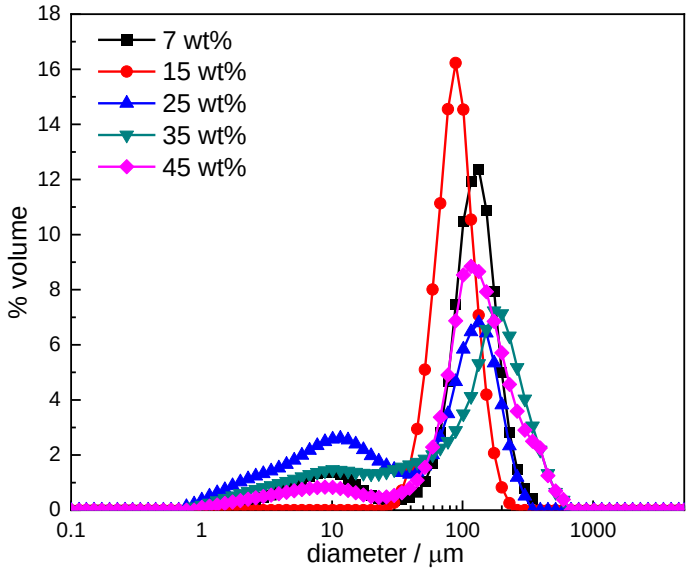

Figure 2: PSD measurements for Ni inks taken after 180 s of sonication for 7, 15, 25, 35 and 45 wt% ionomer.

The PSDs shown in Figure 2 are bimodal for the 7, 25, 35 and 45 wt% samples, showing particles, or rather agglomerates of particles, of around 10 and 100 μm. The 15 wt% sample on the other hand shows a uniform distribution of particles or agglomerates of around 100 μm. This effect could be due to the way the ionomer disperses itself throughout the catalyst ink when the required amount of ionomer to result in 15 wt% on the final electrode layer is used. The fact that the distribution of the 15 wt% electrode is more uniform may be beneficial for a more efficient electrode fabrication as agglomerates can result in clogging or spitting of the air brush when hand-spraying electrodes. It should be noted that the agglomerate size observed in the PSD measurements are representative of the nanoparticles in a catalyst ink containing an ionomer, and as such, will not necessarily correspond to the particle agglomerates observed in the TEM images of the materials. In this case, the agglomerates observed in the PSD measurements of the catalyst inks are larger than what is observed in the TEM images.

3.1.3. Ni Catalyst Coated Surfaces

Samples of the monometallic Ni catalyst coated membranes (CCM) with 7, 15, 25, 35 and 45 wt% ionomer were prepared and evaluated. Images of every CCM after being treated in KOH for 12 h are shown in Figure S5 of the SI. From the images, the 7, 15 and 25 wt% (Figure S5a, b and c, respectively) ionomer electrode surfaces maintain more or less their initial physical form during the ion exchange step, while the structure of the 35 and 45 wt% ionomer electrodes (Figure S5d and e, respectively) have started to break down due to excessive swelling. We therefore consider that an ionomer content of 35 and above is too high for efficient cell operation. Although a higher ionomer content is favoured for improved transport of anions through the catalytic layer, too high of an ionomer content ultimately results in an overhydrated catalytic layer leading to its destruction. Note that initially, the CCM format was going to be used for electrolysis because it is known to be more advantageous due to a lower cell resistances[32], however when using high material loadings on the full 25 cm^2 membrane, the catalytic layer started to peel off once submerged in KOH. This effect can be seen in Figure S6 of the SI. As such, AEMWE experiments were set up using the CCS format.

The physical impact of ionomer content on the catalytic layer morphology was observed with SEM. Representative SEM images of the 7, 15 and 25 wt% ionomer electrode surfaces are shown in Figure 3.

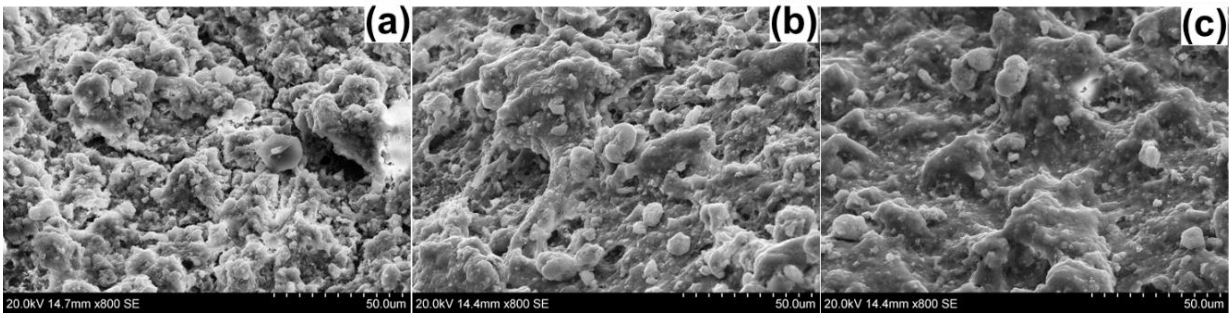

Figure 3: SEM images for (a) 7, (b) 15 and (c) 25 wt% ionomer electrode surfaces.

From inspection of the SEM images, it is possible to see that at lower ionomer concentrations such as the 7 wt% electrode (Figure 3a), the catalytic layer looks more textured and porous. When increasing the ionomer amount, the catalytic layer starts to have less texture and starts to show more agglomerates on its surface. Similar effects of the ionomer on the morphology of catalytic layers have recently been reported[30–34], where electrodes with lower ionomer loadings are less mechanically stable (more cracks) with more access to active sites, and electrodes with higher ionomer content show better mechanical stability with more particle coating and agglomerates. From the SEM images it is possible to say that there is a trade-off between catalytic layer texture and structure, where is more favourable to expose more active sites for oxygen evolution, while the other is more favourable from a durability perspective. However, to properly assess this potential trade-off, in-situ testing of all three electrodes was done and is presented and discussed in the next section.

3.2. In-situ Ionomer Optimization of the Monometallic Ni NPs

The ultimate test for the ionomer optimization is its electrochemical performance. Figure 4 shows IR-corrected polarization curves (Figure 4a) and impedance spectra (Figure 4b) for the 7, 15 and 25 wt% ionomer electrodes prepared using monometallic Ni NPs. The data before IR-correction can be seen in Figure S7 of the SI. Table 2 summarizes key data extracted from Figure

4. The complex-impedance plane plots indicate that an equivalent circuit with at least two relaxations must be used to fit the data. The equivalent circuit should account for charge transfer, adsorption, and double layer capacitance in the porous catalytic layer, although no detailed interpretation is attempted here. After testing a few EIS models, the $LR_{EL}(Q_1R_1)(Q_2R_2)$ circuit is chosen, similar to the one used by Faid *et al.*[25] when studying the hydrogen evolution reaction in the same AEM electrolyser test station. The fitted data is provided so that the first Q_1R_1 parallel represents the high frequency arc, commonly assigned to kinetics contributions at the electrodes, i.e charge transfer (R_{ct}) of both electrodes and a constant phase element that represents the electrode roughness. The second Q_2R_2 parallel represents the low-frequency arc and is commonly assigned to mass transfer and bubble formation [25,53,54]. The R_{EL} represents the uncompensated ohmic resistance, frequently referred to as the high frequency resistance (HFR) and estimated from the real axis approach at high frequency. Finally, the L term represents an inductor term and was added in series to better fit the high frequency data. It should be noted that parameters were only added to the equivalent circuits if it was statistically significant to do so, according to the F-ratio test method[55,56]. Supplementary data for the EIS models are reported in Table S4 of the SI.

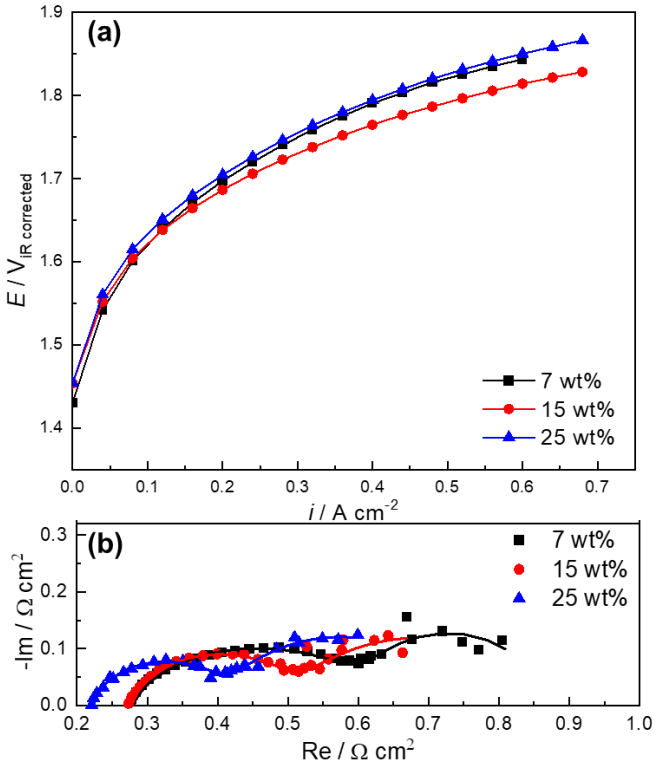

Figure 4: (a) Polarization curves and (b) EIS at 5 A for the monometallic Ni NPs, using 7, 15 and 25 wt% ionomer. Experiments were run at 50°C in 1 M KOH. In (b), the solid lines represent the EIS fit to the equivalent circuit.

Table 2: Summary of polarization and EIS data extracted from Figure 4 for different wt% ionomer.

Ni wt% ionomer	*E* at 0.4 A cm^{-2} [V]	Tafel Impedance [mV]	R_{EL} [mΩ cm^2]	R_1 [mΩ cm^2]	R_2 [mΩ cm^2]
7	1.791	64	254 ± 5	387 ± 19	221 ± 32
15	1.766	48	269 ± 4	354 ± 164	243 ± 29
25	1.793	37	213 ± 3	199 ± 20	338 ± 83

As shown in Figure 4a, the 15 wt% ionomer shows the best catalytic activity by showing a slightly smaller increase in cell potential with increasing current density. At 0.40 A cm^{-2}, it is 250 and 270 mV lower than the 7 and 25 wt% electrodes, respectively. The Ni NPs with 15 wt% ionomer show current densities of 0.280 and 0.538 A cm^{-2} at 1.8 V for the original and IR-corrected graphs,

respectively. This is comparable to what others have found in literature where the ionomer content was optimized for the anode catalytic layer[31–34]. Interestingly, the observation that the ionomer content influences the Ni anode activity is opposite to what Faid *et al.*[36] found in their recent work covering the Fumatech fumion FAA-3 ionomer content optimization for a NiO anode and Ni/C cathode. Through both rotating disc electrode (RDE) measurements and in-situ half-cell AEMWE measurements, Faid *et al.*[36] found that the cathode layer was dependent on the ionomer content, showing an optimal of 10 wt% ionomer, while the anode layer did not show a significant change in activity with varying amounts of ionomer. It should be noted that prior to IR-correction, the 15 and 25 wt% electrodes perform similarly, however this is likely due to the 25 wt% electrode having a thicker catalytic layer, resulting in a more favourable contact between the catalyst layer and the membrane, as further discussed below. To properly factor out effects of cell compression, the IR-corrected polarization curves were used to identify the optimal amount of ionomer.

As for the impedance spectra in Figure 4b, for an increasing ionomer content, the first semicircle resistance (R_1) decreases. Park *et al.* [32] found a similar change in charge transfer resistance with increasing ionomer content, and attributed this effect to the increased size of secondary pores. The second semicircle resistance (R_2) increases with increasing ionomer content, which could be attributed to large quantities of ionomer inhibiting mass transport. The 25 wt% ionomer shows a noticeably lower ohmic resistance (R_{EL}) than the 7 and 15 wt% electrodes. Interestingly, a lower ohmic resistance for the 25 wt% ionomer electrode was observed despite a thicker catalyst layer. This is in line with the observed reduced ohmic resistance that Faid *et al.*[25] observed when employing a NiMo/C catalyst instead of a Pt/C catalyst for the hydrogen evolution reaction in the same set-up using 1 M KOH. In addition to the electrolyte resistance, constriction or contact resistances, ohmic resistance in pores and pore distribution, as well as uneven reaction

distribution will contribute to the impedance spectra and impact the measured high frequency resistance. Furthermore, Tafel impedances were extracted from the impedance measurements as the diameter of the impedance arc, assuming only kinetic contributions (i.e. subtracting the ohmic resistance from the impedance spectra and multiplying it with the steady state current [57,58]). This showed that the 25 wt% sample led to the lowest Tafel slope of 37 mV. The validity of the Tafel impedance calculations may however be questioned as the low frequency tail observed, likely due to bubble formation or mass transport[53], was not taken into account.

After AEMWE testing was completed, the cells were opened and the anode catalytic layer residue on the membrane (anode catalytic layer that broke off the carbon paper) was observed. This is shown in Figure 5 for all 3 samples. From the images, it is possible to observe that the 15 wt% ionomer layer (Figure 5b) lost the least amount of material. The 7 wt% layer (Figure 5a) did not have enough ionomer to bind the catalytic layer, causing it to detach when the parallel flow field was pressed into it, and the 25 wt% layer (Figure 5c) was over hydrated during electrolysis causing the catalytic layer to partially disintegrate. In other words, the 15 wt% ionomer electrode was the only one that had: (i) enough ionomer to keep all the particles adhered to the GDL, despite the imposed shear stress, which causes the particles to be forced off the catalytic layer, and (ii) not too much ionomer to cause excessive swelling and thus loss of the catalytic layer structure. The effects of swelling with increased ionomer content are also apparent on the MEAs that were made, then exchanged in 1 M KOH in Figure S5 of the SI. As such, although the 15 and 25 wt% ionomer electrodes both showed good performance, the 15 wt% showed a better adhesion of the catalytic layer and was therefore chosen as the optimal ionomer content for the Ni-based materials. It is important to note that observing the state of the anode GDL post-testing is only a preliminary indicator of the efficiency of catalytic layer under operating conditions. Running electrolysis for

thousands of hours under various conditions would be required to truly put the mechanical durability of an electrode to the test.

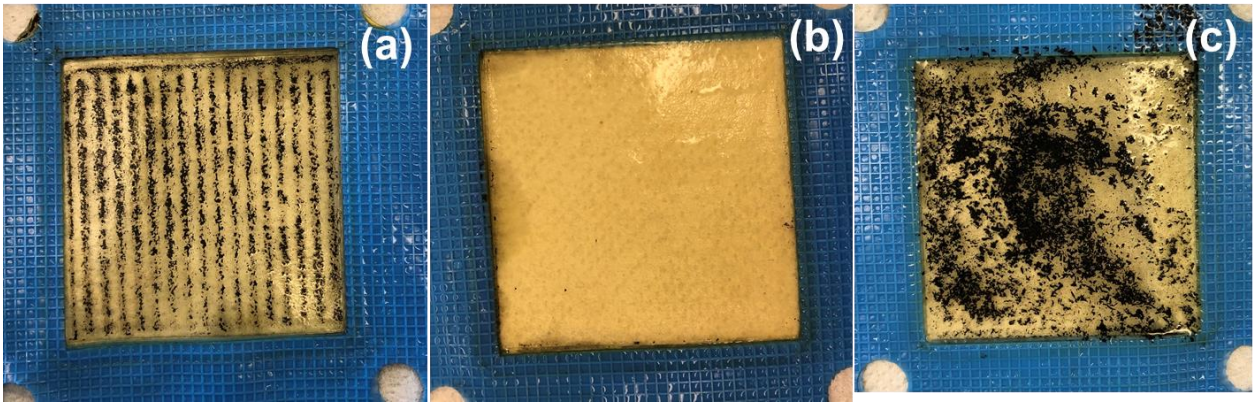

Figure 5: Anode catalytic residue on the AEM after electrolysis for (a) 7, (b) 15 and (c) 25 wt% ionomer.

3.3. AEMWE Performance Evaluation of the Ni-based NPs

3.3.1. Polarization Curves and Electrochemical Impedance

Once the ionomer content for the Ni electrodes was optimized, the 15 wt% ionomer content was used when fabricating the anodes for the $Ni_{90}Fe_{10}$, $Ni_{80}Fe_{20}$, $Ni_{90}Fe_{10}$/10 wt% CeO_2 and $Ni_{80}Fe_{20}$/10 wt% CeO_2 catalysts. Figure 6 shows polarization curves (Figure 6a, b) and EIS measurements (Figure 6c, d) for all the mentioned Ni-based materials in addition to the Ir black benchmark catalyst in 1 (Figure 6a, c) and 0.1 (Figure 6b, d) M KOH. Tables 3 and 4 summarize key information extracted from the plots in Figure 6 in 1 and 0.1 M KOH, respectively. To see polarization curves without IR-correction, see Figure S8 in the SI. The EIS data for the materials tested in 1 and 0.1 M KOH were analyzed using a similar equivalent circuit as the ionomer optimization study. Here however, it was not always statistically significant to use a more complex circuit, such as the $LR_{EL}(Q_1R_1)(Q_2R_2)$ model described above. In some cases, the circuit was not improved by adding the inductor term, *L*, and in other cases, a simple $R_{EL}(QR_P)$ circuit best fit the experimental data. In the latter case, the polarization resistance R_P would represent both the

previous R_1 and R_2. For data of the best fitted EIS models in 1 and 0.1 M KOH, see Table S5 and S6, respectively, in the SI.

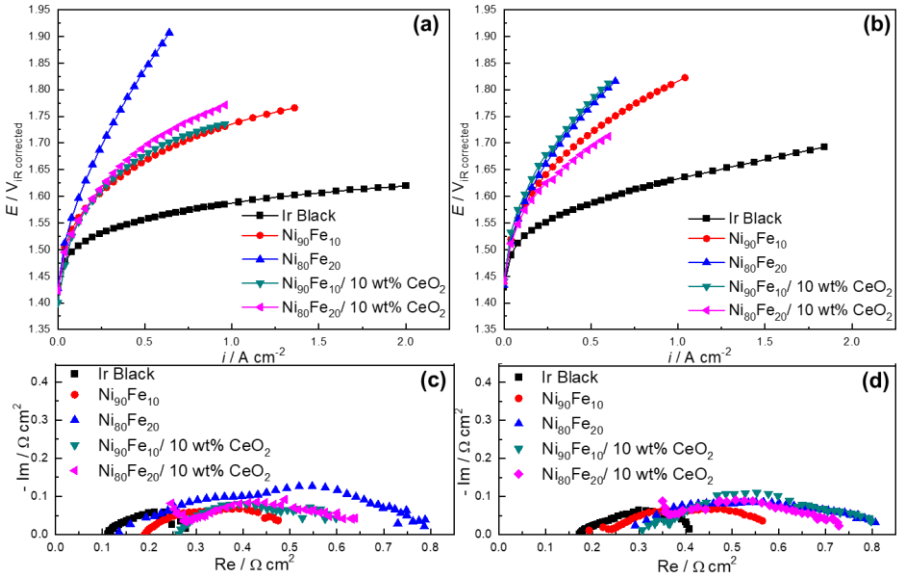

Figure 6: Polarization curves (a, b) and electrochemical impedance spectroscopy run at 5 A (c, d) run in 1 (a, c) and 0.1 (b, d) M KOH at 50°C.

Table 3: Summary of in-situ performance in 1 M KOH extracted from Figure 6a and c.

Material	***E* at 0.4 A cm^{-2} [V]**	***E* at 0.8 A cm^{-2} [V]**	**Tafel Impedance [mV]**	**R_{EL} [mΩ cm^2]**
Ir Black	1.547	1.578	34	109 ± 1
$Ni_{90}Fe_{10}$	1.645	1.717	63	170 ± 3
$Ni_{80}Fe_{20}$	1.785	N/A	131	130 ± 10*
$Ni_{90}Fe_{10}$/10 wt% CeO_2	1.655	1.723	70	250 ± 3
$Ni_{80}Fe_{20}$/10 wt% CeO_2	1.688	1.751	73	232 ± 6

*It should be noted that this value may be misrepresenting the actual R_{EL} of the system because the impedance of this sample in the high frequency region is not ideal. See the SI for more details.

Table 4: Summary of in-situ performance in 0.1 M KOH extracted from Figure 6b and d.

Material	***E* at 0.4 A cm^{-2} [V]**	***E* at 0.8 A cm^{-2} [V]**	**Tafel Impedance [mV]**	**R_{EL} [mΩ cm^2]**
Ir Black	1.577	1.617	47	158 ± 12
$Ni_{90}Fe_{10}$	1.692	1.782	70	220 ± 2
$Ni_{80}Fe_{20}$	1.732	N/A	108	144 ± 32*
$Ni_{90}Fe_{10}$/10 wt% CeO_2	1.743	N/A	102	314 ± 9
$Ni_{80}Fe_{20}$/10 wt% CeO_2	1.666	N/A	74	338 ± 5

*It should be noted that this value may be misrepresenting the actual R_{EL} of the system because the impedance of this sample in the high frequency region is not ideal.

In 1 M KOH, Ir black is the best performing electrode showing voltages of around 1.58 at 0.8 A cm^{-2}. This is closely followed by $Ni_{90}Fe_{10}$ showing a cell voltage of 1.72 V at that same current. The ceria containing materials are not too far behind the $Ni_{90}Fe_{10}$ performance, where the $Ni_{90}Fe_{10}$/10 wt% CeO_2 electrode outperforms the $Ni_{80}Fe_{20}$/10 wt% CeO_2. The $Ni_{80}Fe_{20}$ is the least performing catalyst, which is unexpected considering it shows better three-electrode cell OER performance than all other Ni-based materials in this study[46]. It is however important to note that although a catalyst presents high activity in a three-electrode cell, it will not necessarily show high performance in an electrolyser, as discussed in the works of Xu *et al.*[18]. Additionally, it is known that iron is not stable at the anode in electrolyser systems[59], therefore it is possible that here, the stability of the $Ni_{80}Fe_{20}$ electrode is lower due to its higher iron content.

In the EIS data shown in Figure 6c, the lowest ohmic resistance of around 109 mΩ cm^2 was found for the Ir electrode, with the $Ni_{80}Fe_{20}$ electrode showing the next the lowest ohmic resistance of around 130 mΩ cm^2. Overall, the samples containing 20 at% Fe show lower electrolyte resistances than their 10 at% Fe equivalents. Additionally, while we have dramatically reduced the ceria content from 50 to 10 wt% following our previous AEMWE study[26], the ceria containing samples still show higher R_{EL} values than their metallic equivalent. This result is in agreement with

our recent detailed ex-situ study on the effects of CeO_2 on the OER performance of NiFe nanoparticles[46], where we find that while CeO_2 can be beneficial to electrochemical performance, it also introduces additional ohmic resistances to the catalyst, which can lower its overall catalytic activity. It is important to note that while poor conductivity and constriction resistance between electrical and ionic conductors, as well as electrolyte solution resistance can affect the R_{EL}, the observed changes in R_{EL} with different catalyst materials are likely more importantly related to changes in the resistance of the electrolyte solution within the system.

In terms of the charge transfer resistance shown in Figure 6c, Ir black has the lowest resistance of 132 mΩ cm^2, followed by $Ni_{90}Fe_{10}$/ 10 wt% CeO_2, which has a resistance of around 242 mΩ cm^2. Overall, the 10 at% iron samples show lower observed polarization resistances than their 20 at% Fe equivalents. When preparing the CCS of the materials containing 20 at% iron, the material was readily oxidizing. This effect, in combination with the aforementioned possible low stability of Fe in the $Ni_{80}Fe_{20}$ catalyst, could be negatively affecting AEMWE performance and the observed polarization resistance. The low relative activity of the $Ni_{80}Fe_{20}$ electrode is reflected in its extremely high charge transfer resistance of 774 mΩ cm^2. The $Ni_{80}Fe_{20}$ electrode also shows a Tafel impedance value of 131 mV, 58 mV higher than any other electrode. With respects to the ceria-containing materials, they each show lower observed polarization resistances than their metallic equivalents, possibly due to electronic effects that ceria has on NiFe. This result is in accordance with our previous work[26], showing that ceria has beneficial effects on the charge transfer of the process.

In 0.1 M KOH, the iridium electrode still shows the best performance in terms of lowest reaction overpotential and low cell resistances. Aside from Ir, the only other material to reach 0.8 A cm^{-2} was $Ni_{90}Fe_{10}$, which shows a cell voltage of 1.78 V at that current, which is 165 mV higher

than what was obtained for Ir. Interestingly, in 0.1 M KOH, the $Ni_{80}Fe_{20}$/10 wt% CeO_2 electrode shows the best performance of all Ni-based materials, showing a cell voltage of 1.67 V at 0.4 A cm^{-2} after IR-correction. It also shows a low charge transfer resistance in comparison to $Ni_{80}Fe_{20}$ and $Ni_{90}Fe_{10}$/ 10 wt% CeO_2. Reasons for the change in relative behaviour of the $Ni_{80}Fe_{20}$/ 10 wt% ceria electrode with pH, could be related to ceria's oxygen storage capacity and reducibility, which may favourably affect the local pH in the vicinity of the electrode, improving electrochemical activity. While this effect is likely also present in the $Ni_{90}Fe_{10}$/ 10 wt% CeO_2, it is possible that having more Fe in comparison to Ni in the $Ni_{80}Fe_{20}$/ 10 wt% CeO_2 material, alters the properties of the catalyst to further boost the surface oxygen ion (O^{2-}) conductivity of ceria, making it outperform $Ni_{90}Fe_{10}$/ 10 wt% CeO_2 in 0.1 M KOH. It should be noted that prior to IR-correction, $Ni_{90}Fe_{10}$ was the best performing Ni-based electrode, followed by the $Ni_{80}Fe_{20}$/ 10% CeO_2. This is illustrated in Figure S8.

Overall, the $Ni_{90}Fe_{10}$ electrode is the best Ni-based AEMWE anode, however, when analyzing the IR-corrected data in 0.1 M KOH, the $Ni_{80}Fe_{20}$/10 wt% CeO_2 outperforms $Ni_{90}Fe_{10}$. Recalling the results of the BET measurements of the respective catalyst powders, the $Ni_{90}Fe_{10}$ has a low BET area but a high average pore size, while the $Ni_{80}Fe_{20}$/10 wt% CeO_2 has a high BET area with a low average pore size. It could therefore be said that at the higher electrolyte concentrations, it is more important to have larger pores to allow for better mass and ion transport through the catalytic layer, while at lower concentrations, it is more important to have a higher area to expose more active sites. It would of course be ideal to combine having a large average pore size with a high BET area to expose the most active sites, while allowing for optimal ion and mass transport through the catalytic layer.

Overall, although a direct comparison cannot be made due to many different cell variables, it is possible to say that these results are comparable to what has previously been reported in literature[6,32,60–63]. Based on the above results in both 1 and 0.1 M KOH, it is not evident whether incorporating ceria into the catalyst helps very much with performance. The ceria-containing materials have a larger high frequency resistance, which makes their IR-corrected catalytic performance more comparable to the other catalysts. When looking at the actual electrode loadings reported in Table S1 of the SI, both the $Ni_{90}Fe_{10}$/10 wt%CeO_2 and $Ni_{80}Fe_{20}$/10 wt% CeO_2 materials have a lower loading than their metallic counterpart. It could therefore be possible that the lower performance of those materials was due to the lower resulting anode loadings. Interestingly, in most cases, the addition of CeO_2 to the $Ni_{90}Fe_{10}$ and $Ni_{80}Fe_{20}$ materials results in a lower charge transfer resistance indicating more favourable kinetics.

3.3.2. Electrode Stability

Many authors[10,18,31,64–67] have done durability investigations of their systems for times ranging from hours to days of operation. In this study, preliminary durability measurements were performed over 12 h on the Ni-based catalysts to see how well their performance holds over time in an AEMWE setup. This can be seen in Figure 7 with key information of that plot presented in Table 5.

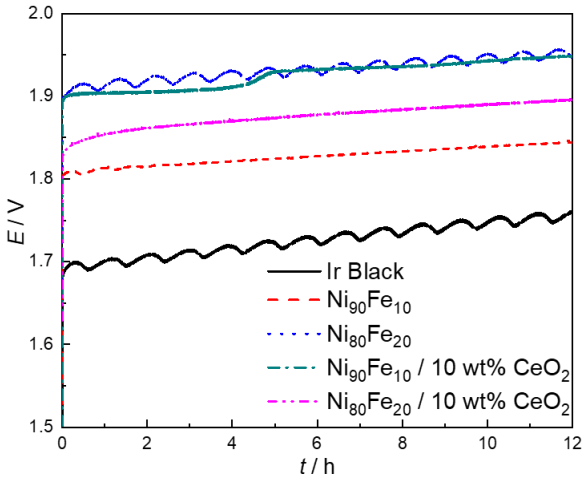

Figure 7: Chronopotentiometry (CP) experiments at 0.5 A cm^{-2} in 0.1 M KOH at 50°C. Catalysts: Ir black, $Ni_{90}Fe_{10}$, $Ni_{80}Fe_{20}$, $Ni_{90}Fe_{10}$/ 10 wt% CeO_2 and $Ni_{80}Fe_{20}$/ 10 wt% CeO_2.

Table 5: Summary of in-situ stability performance evaluation in 0.1 M KOH extracted from Figures 7 and 8.

Material	**ΔE [mV]**	**Degradation Rate [mV h^{-1}]**	**ΔTafel Impedance [mV]**
Ir Black	67	5.6	16
$Ni_{90}Fe_{10}$	40	3.3	3
$Ni_{80}Fe_{20}$	47	3.9	5
$Ni_{90}Fe_{10}$/10 wt% CeO_2	52	4.3	4
$Ni_{80}Fe_{20}$/10 wt% CeO_2	62	5.2	3

In addition to the long-term polarization, an EIS spectrum was taken every hour during the 12 hour polarization experiment. Figure 8 shows the spectrum taken at the 1st, 6th and 12th hour for every material. The change in Tafel impedance over 12 hours is reported in Table 5. To see the EIS spectra taken every hour, see Figure S9 in the SI. See Table S7 of the SI for the best fitted EIS models for the spectra shown in Figure 8 at hours 1 and 12.

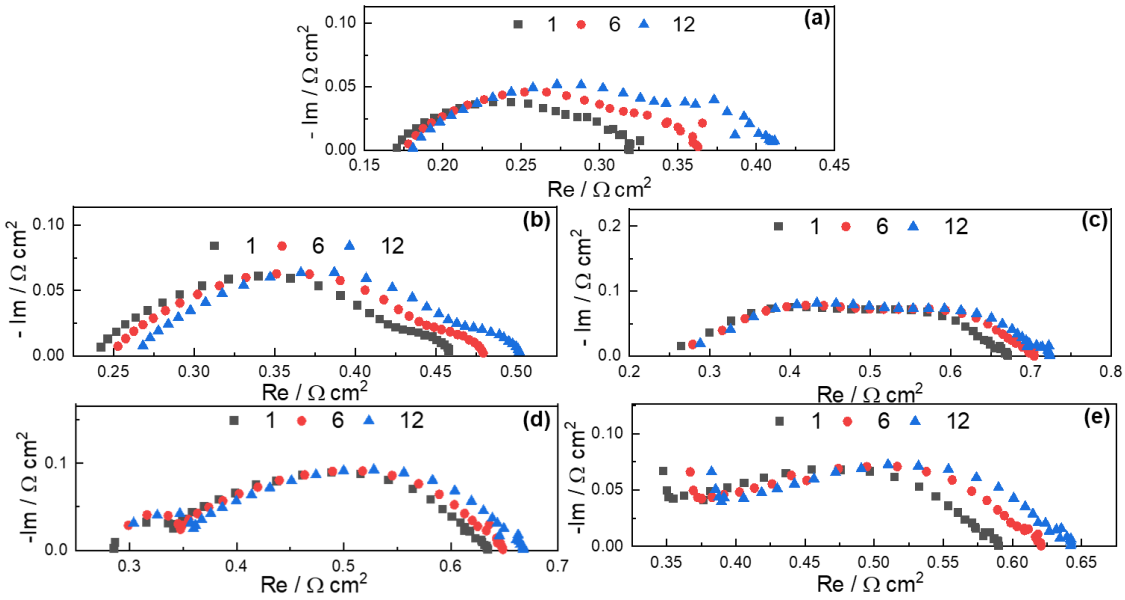

Figure 8: Electrochemical impedance spectroscopy of (a) Ir black, (b) $Ni_{90}Fe_{10}$, (c) $Ni_{80}Fe_{20}$, (d) $Ni_{90}Fe_{10}$/10 wt% CeO_2 and (e) $Ni_{80}Fe_{20}$/10 wt% CeO_2 taken at the 1st, 6th and 12th hour of polarization.

As shown in Figure 7, the best performing material in terms of lowest cell potential is Ir black, which is followed by $Ni_{90}Fe_{10}$ and then $Ni_{80}Fe_{20}$/10 wt% CeO_2. This is as expected following the results of the polarization experiments presented above. As shown in Table 5, although the Ir benchmark shows the lowest current, its change in potential over the 12 hours is higher than all Ni-based materials, likely due to its low stability in an alkaline environment[68]. Based on the calculated degradation rate, it could be possible that over a longer period, the Ni-based electrodes would outperform Ir black. Overall, the materials containing 10 at% iron are more stable that their 20 at% iron equivalents, where the most stable Ni-based material is the $Ni_{90}Fe_{10}$ catalyst showing a change in voltage of 40 mV over 12 hours or a degradation rate of 3.3 mV h^{-1}. It should be noted that a degradation rate of 3.3 mV h^{-1} is not practical for commercial scale operation. An example of an AEMWE that shows a more commercially stable performance is presented in the works of Motealleh *et al.*[67], where they run electrolysis testing for 10 000 h at 1 A/cm^2. Their cell, constructed using a Sustainion® membrane and Ni-based anodes and cathode, is able to hold

around 1.85 V over 10 000 h at 60°C in 1 M KOH, showing a degradation rate of less than 1 μV h^{-1}. Incorporating ceria into the $Ni_{90}Fe_{10}$ and $Ni_{80}Fe_{20}$ catalysts did not help the catalysts' overall stability as both materials with ceria showed higher degradation rates than their respective metallic counterpart. These stability results are all in accordance with the results found in our three-electrode study for the NiFe materials with and without 10 wt% ceria[46].

The observed positive degradation rate of the NiFe materials without ceria shown in Figure 7 could be due to iron dissolution under applied currents[59] and could be more important for the samples with 20 at% Fe. As for the materials containing ceria, a possible reason for this decrease in stability over time could be the phase segregation of a redox inactive CeO_2 phase[38,69,70], however a more detailed investigation into the interactions of Ni, Fe and CeO_2 under constant applied current would need to be done to know for sure. Additionally, while short term durability testing can be informative, running longer durability experiments (over thousands of hours) would be required to know whether the voltage drift observed in Figure 7 is maintained over time.

When analyzing the EIS data in Figure 8, all materials have an increase in the ohmic resistance over time. Furthermore, contrary to the ceria containing materials, the Ir black, $Ni_{90}Fe_{10}$ and $Ni_{80}Fe_{20}$ cells seem to have a more prominent second semicircle with time. This could mean that incorporating ceria into the catalysts helps with the transport of water to the surface and the bubble release from the surface allowing for more consistent mass transfer overtime, all while maintaining the integrity of the pores in the catalytic layer. The Ir black electrode also shows the largest increase in observed polarization resistance over time, possibly related to its higher degradation rate in comparison to the Ni-based materials.

4. Conclusions

In this work, we have determined the optimal amount of commercial Fumatech anionic ionomer content to be 15 wt% in $Ni_{90}Fe_{10}$ and $Ni_{80}Fe_{20}$ NPs, both with and without 10% CeO_2 catalysts for the oxygen evolution reaction in anion exchange membrane water electrolysis (AEMWE). The optimization was based on particle size distribution measurements of the catalyst inks, scanning electro microscopy images of the prepared electrode surfaces and electrochemical performance in an operating AEMWE single cell. 15 wt% ionomer provided the highest activity, while showing the best adhesion of the catalyst particles within the catalytic layer. The $Ni_{90}Fe_{10}$ and $Ni_{80}Fe_{20}$ NPs with and without 10% CeO_2 catalysts were evaluated using the optimal 15 wt% ionomer. $Ni_{90}Fe_{10}$ is found to be the best-performing non-noble metal catalyst, showing 1.72 V at 0.8 A cm^{-2} in 1 M KOH after IR-correction. However, in 0.1 M KOH the $Ni_{80}Fe_{20}$/10 wt% CeO_2 catalyst obtained a higher activity than $Ni_{90}Fe_{10}$, achieving an IR-corrected cell voltage of 1.67 V at 0.4 A cm^{-2}. This increase in relative activity of the $Ni_{80}Fe_{20}$/ 10 wt% CeO_2 electrode at lower pH, could be due to ceria's oxygen storage capacity and reducibility. Based on the calculated degradation rates during stability measurements, it is likely that the Ni-based electrodes, particularly the $Ni_{90}Fe_{10}$ electrode, will outperform Ir black when operated over an extended period. Upon measuring electrochemical impedance over the course of the durability experiments, it was observed that incorporating ceria into electrodes may assist mass transport within the catalytic layer over time perhaps by maintaining the porous structure of the catalytic layer.

5. Acknowledgements

This research was conducted as part of the Engineered Nickel Catalysts for Electrochemical Clean Energy project administered from Queen's University and supported by Grant number RGPNM 477963-2015 under the Natural Sciences and Engineering Research Council of Canada (NSERC) Discovery Frontiers Program. This work was also carried out within the HAPEEL project "Hydrogen Production by Alkaline Polymer Electrolyte Electrolysis," financially supported by the Research Council of Norway-ENERGIX program, contract number 268019. Additionally, the Research Council of Norway is acknowledged for the support to the Norwegian Fuel cell and Hydrogen Centre and the INTPART project 261620. Finally, funding was also provided by NSERC's Alexander Graham Bell Canada Graduate Scholarship – Doctoral (CGS D).

6. References

[1] D.M.F. Santos, C.A.C. Sequeira, Hydrogen Production by Alkaline Water Electrolysis, Quim. Nova. 36 (2013) 1176–1193. doi:10.1109/ICACCI.2017.8125843.

[2] M. Carmo, D.L. Fritz, J. Mergel, D. Stolten, A comprehensive review on PEM water electrolysis, Int. J. Hydrogen Energy. 38 (2013) 4901–4934. doi:10.1016/j.ijhydene.2013.01.151.

[3] K. Zeng, D. Zhang, Recent progress in alkaline water electrolysis for hydrogen production and applications, Prog. Energy Combust. Sci. 36 (2010) 307–326. doi:10.1016/j.pecs.2009.11.002.

[4] J. Turner, G. Sverdrup, M.K. Mann, P.-C. Maness, B. Kroposki, M. Ghirardi, R.J. Evans, D. Blake, Renewable hydrogen production, Int. J. Energy Res. 32 (2008) 379–407. doi:10.1002/er.

[5] R. Phillips, A. Edwards, B. Rome, D.R. Jones, C.W. Dunnill, Minimising the ohmic resistance of an alkaline electrolysis cell through effective cell design, Int. J. Hydrogen Energy. 42 (2017) 23986–23994. doi:10.1016/j.ijhydene.2017.07.184.

[6] Y. Leng, G. Chen, A.J. Mendoza, T.B. Tighe, M.A. Hickner, C.-Y. Wang, Solid-State Water Electrolysis with an Alkaline Membrane, J. Am. Chem. Soc. 134 (2012) 9054−9057. doi:10.1021/ja302439z.

[7] M.M. Rashid, M.K. Al Mesfer, H. Naseem, M. Danish, Hydrogen Production by Water Electrolysis: A Review of Alkaline Water Electrolysis, PEM Water Electrolysis and High Temperature Water Electrolysis, Int. J. Eng. Adv. Technol. (2015) 2249–8958.

[8] M. Bodner, A. Hofer, V. Hacker, H2 generation from alkaline electrolyzer, Wiley Interdiscip. Rev. Energy Environ. 4 (2015) 365–381. doi:10.1002/wene.150.

[9] D. Pletcher, X. Li, Prospects for alkaline zero gap water electrolysers for hydrogen production, Int. J. Hydrogen Energy. 36 (2011) 15089–15104. doi:10.1016/j.ijhydene.2011.08.080.

[10] S. Marini, P. Salvi, P. Nelli, R. Pesenti, M. Villa, M. Berrettoni, G. Zangari, Y. Kiros, Advanced alkaline water electrolysis, Electrochim. Acta. 82 (2012) 384–391. doi:10.1016/j.electacta.2012.05.011.

[11] I. Vincent, D. Bessarabov, Low cost hydrogen production by anion exchange membrane electrolysis: A review, Renew. Sustain. Energy Rev. 81 (2018) 1690–1704. doi:10.1016/j.rser.2017.05.258.

[12] M.K. Cho, A. Lim, S.Y. Lee, H. Kim, S.J. Yoo, Y. Sung, H.S. Park, J.H. Jang, A Review on Membranes and Catalysts for Anion Exchange Membrane Water Electrolysis Single Cells, J. Electrochem. Sci. Technol. 8 (2017) 183–196. doi:10.5229/JECST.2017.8.3.183.

[13] M. David, C. Ocampo-martínez, R. Sánchez-peña, Advances in alkaline water electrolyzers : A review, J. Energy Storage. 23 (2019) 392–403. doi:10.1016/j.est.2019.03.001.

[14] R. Phillips, C.W. Dunnill, Zero gap alkaline electrolysis cell design for renewable energy storage as hydrogen gas, RSC Adv. 6 (2016) 100643–100651. doi:10.1039/C6RA22242K.

[15] H.A. Miller, K. Bouzek, J. Hnat, S. Loos, C.I. Bernäcker, T. Weißgärber, L. Röntzsch, J. Meier-Haack, Green hydrogen from anion exchange membrane water electrolysis: A review of recent developments in critical materials and operating conditions, Sustain. Energy Fuels. 4 (2020) 2114. doi:10.1039/c9se01240k.

[16] D. Henkensmeier, M. Najibah, C. Harms, J. Žitka, J. Hnát, K. Bouzek, Overview: State-of-the Art Commercial Membranes for Anion Exchange Membrane Water Electrolysis, J. Electrochem. Energy Convers. Storage. 18 (2021). doi:10.1115/1.4047963.

[17] M.E.G. Lyons, R.L. Doyle, M.P. Browne, I.J. Godwin, A.A.S. Rovetta, Recent developments in electrochemical water oxidation, Curr. Opin. Electrochem. 1 (2017) 40–45. doi:10.1016/j.coelec.2016.12.005.

[18] D. Xu, M.B. Stevens, M.R. Cosby, S.Z. Oener, A.M. Smith, L.J. Enman, K.E. Ayers, C.B. Capuano, J.N. Renner, N. Danilovic, Y. Li, H. Wang, Q. Zhang, S.W. Boettcher, Earth-Abundant Oxygen Electrocatalysts for Alkaline Anion-Exchange-Membrane Water Electrolysis: Effects of Catalyst Conductivity and Comparison with Performance in Three-Electrode Cells, ACS Catal. 9 (2019) 7–15. doi:10.1021/acscatal.8b04001.

[19] P. Du, R. Eisenberg, Catalysts made of earth-abundant elements (Co, Ni, Fe) for water splitting: Recent progress and future challenges, Energy Environ. Sci. 5 (2012) 6012–6021. doi:10.1039/c2ee03250c.

[20] M. Tahir, L. Pan, F. Idrees, X. Zhang, L. Wang, J.J. Zou, Z.L. Wang, Electrocatalytic oxygen evolution reaction for energy conversion and storage: A comprehensive review, Nano Energy. 37 (2017) 136–157. doi:10.1016/j.nanoen.2017.05.022.

[21] F. Safizadeh, E. Ghali, G. Houlachi, Electrocatalysis developments for hydrogen evolution reaction in alkaline solutions - A Review, Int. J. Hydrogen Energy. 40 (2015) 256–274. doi:10.1016/j.ijhydene.2014.10.109.

[22] M. Gong, H. Dai, A mini review of NiFe-based materials as highly active oxygen evolution reaction electrocatalysts, Nano Res. 8 (2015) 23–39. doi:10.1007/s12274-014-0591-z.

[23] M. Gong, D.Y. Wang, C.C. Chen, B.J. Hwang, H. Dai, A mini review on nickel-based electrocatalysts for alkaline hydrogen evolution reaction, Nano Res. 9 (2016) 28–46. doi:10.1007/s12274-015-0965-x.

[24] M. Schalenbach, O. Kasian, K.J.J. Mayrhofer, An alkaline water electrolyzer with nickel electrodes enables efficient high current density operation, Int. J. Hydrogen Energy. 43 (2018) 11932–11938. doi:10.1016/j.ijhydene.2018.04.219.

[25] A. Faid, A. Oyarce Barnett, F. Seland, S. Sunde, Highly Active Nickel-Based Catalyst for Hydrogen Evolution in Anion Exchange Membrane Electrolysis, Catalysts. 8 (2018) 614. doi:10.3390/catal8120614.

[26] E. Cossar, A.O. Barnett, F. Seland, E.A. Baranova, The Performance of Nickel and Nickel-Iron Catalysts Evaluated as Anodes in Anion Exchange Membrane Water Electrolysis, Catalysts. 9 (2019) 814.

[27] J.H. Kim, J.N. Lee, C.Y. Yoo, K.B. Lee, W.M. Lee, Low-cost and energy-efficient asymmetric nickel electrode for alkaline water electrolysis, Int. J. Hydrogen Energy. 40 (2015) 10720–10725. doi:10.1016/j.ijhydene.2015.07.025.

[28] Z. Chen, C.X. Kronawitter, X. Yang, Y.W. Yeh, N. Yao, B.E. Koel, The promoting effect of tetravalent cerium on the oxygen evolution activity of copper oxide catalysts, Phys. Chem. Chem. Phys. 19 (2017) 31545–31552. doi:10.1039/c7cp05248k.

[29] J.R. Varcoe, P. Atanassov, D.R. Dekel, A.M. Herring, M.A. Hickner, P.A. Kohl, A.R. Kucernak, W.E. Mustain, K. Nijmeijer, K. Scott, T. Xu, L. Zhuang, Anion-exchange membranes in electrochemical energy systems, Energy Environ. Sci. 7 (2014) 3135–3191. doi:10.1039/c4ee01303d.

[30] G.-F. Li, D. Yang, P.Y.A. Chuang, Defining Nafion Ionomer Roles for Enhancing Alkaline Oxygen Evolution Electrocatalysis, ACS Catal. 8 (2018) 11688. doi:10.1021/acscatal.8b02217.

[31] I. Vincent, A. Kruger, D. Bessarabov, Development of efficient membrane electrode assembly for low cost hydrogen production by anion exchange membrane electrolysis, Int. J. Hydrogen Energy. 42 (2017) 10752–10761. doi:10.1016/j.ijhydene.2017.03.069.

[32] J.E. Park, S.Y. Kang, S.H. Oh, J.K. Kim, M.S. Lim, C.Y. Ahn, Y.H. Cho, Y.E. Sung, High-performance anion-exchange membrane water electrolysis, Electrochim. Acta. 295 (2019) 99–106. doi:10.1016/j.electacta.2018.10.143.

[33] M.K. Cho, H. Park, S. Choe, S.J. Yoo, J.Y. Kim, H.-J. Kim, D. Henkensmeier, S.Y. Lee, Y. Sung, H.S. Park, J. Hyun Jang, Factors in electrode fabrication for performance enhancement of anion exchange membrane water electrolysis, J. Power Sources. 347 (2017) 283–290. doi:10.1016/j.jpowsour.2017.02.058.

[34] M.K. Cho, H.Y. Park, H.J. Lee, H.J. Kim, A. Lim, D. Henkensmeier, S.J. Yoo, J.Y. Kim, S.Y. Lee, H.S. Park, J.H. Jang, Alkaline anion exchange membrane water electrolysis: Effects of electrolyte feed method and electrode binder content, J. Power Sources. 382 (2018) 22–29. doi:10.1016/j.jpowsour.2018.02.025.

[35] T.W. Koo, C.S. Park, Y. Do Kim, D. Lee, S. Park, J.H. Lee, S.M. Choi, C.Y. Choi, Oxygen Evolution Reaction Characteristics of Synthetic Nickel-cobalt-oxide Electrodes for Alkaline Anion-exchange Membrane Water Electrolysis, J. Korean Phys. Soc. 67 (2015) 1558–1562. doi:10.3938/jkps.67.1558.

[36] A.Y. Faid, L. Xie, A.O. Barnett, F. Seland, D. Kirk, S. Sunde, Effect of anion exchange ionomer content on electrode performance in AEM water electrolysis, Int. J. Hydrogen Energy. 45 (2020) 28272–28284. doi:10.1016/j.ijhydene.2020.07.202.

[37] M.K. Bates, Q. Jia, N. Ramaswamy, R.J. Allen, S. Mukerjee, Composite Ni/NiO-Cr2O3 catalyst for alkaline hydrogen evolution reaction, J. Phys. Chem. C. 119 (2015) 5467–5477. doi:10.1021/jp512311c.

[38] L.J. Enman, M.S. Burke, A.S. Batchellor, S.W. Boettcher, Effects of Intentionally Incorporated Metal Cations on the Oxygen Evolution Electrocatalytic Activity of Nickel (Oxy)hydroxide in Alkaline Media, ACS Catal. 6 (2016) 2416–2423.

doi:10.1021/acscatal.5b02924.

[39] C.C.L. McCrory, S. Jung, J.C. Peters, T.F. Jaramillo, Benchmarking heterogeneous electrocatalysts for the oxygen evolution reaction, J. Am. Chem. Soc. 135 (2013) 16977–16987. doi:10.1021/ja407115p.

[40] S. Lee, L. Bai, X. Hu, Deciphering Iron-Dependent Activity in Oxygen Evolution Catalyzed by Nickel – Iron Layered Double Hydroxide, Angew. Chemie - Int. Ed. 59 (2020) 8072. doi:10.1002/ange.201915803.

[41] L. Trotochaud, J.K. Ranney, K.N. Williams, S.W. Boettcher, Solution-cast metal oxide thin film electrocatalysts for oxygen evolution, J. Am. Chem. Soc. 134 (2012) 17253–17261. doi:10.1021/ja307507a.

[42] M.B. Stevens, C.D.M. Trang, L.J. Enman, J. Deng, S.W. Boettcher, Reactive Fe-Sites in Ni/Fe (Oxy)hydroxide Are Responsible for Exceptional Oxygen Electrocatalysis Activity, J. Am. Chem. Soc. 139 (2017) 11361−11364. doi:10.1021/jacs.7b07117.

[43] D. Friebel, M.W. Louie, M. Bajdich, K.E. Sanwald, Y. Cai, A.M. Wise, M. Cheng, D. Sokaras, T. Weng, R. Alonso-mori, R.C. Davis, J.R. Bargar, J.K. Nørskov, A. Nilsson, A.T. Bell, Identification of Highly Active Fe Sites in (Ni,Fe)OOH for Electrocatalytic Water Splitting, J. Am. Chem. Soc. 137 (2015) 1305. doi:10.1021/ja511559d.

[44] J.-X. Feng, S.-H. Ye, H. Xu, Y.-X. Tong, G.-R. Li, Design and Synthesis of FeOOH/CeO 2 Heterolayered Nanotube Electrocatalysts for the Oxygen Evolution Reaction , Adv. Mater. 28 (2016) 4698–4703. doi:10.1002/adma.201600054.

[45] J.A. Haber, Y. Cai, S. Jung, C. Xiang, S. Mitrovic, J. Jin, A.T. Bell, J.M. Gregoire, Discovering Ce-rich oxygen evolution catalysts, from high throughput screening to water electrolysis, Energy Environ. Sci. 7 (2014) 682–688. doi:10.1039/c3ee43683g.

[46] E. Cossar, K. Agarwal, V.B. Nguyen, R. Safari, G.A. Botton, E.A. Baranova, Highly Active Nickel–Iron Nanoparticles With and Without Ceria for the Oxygen Evolution Reaction, Electrocatalysis. (2021). doi:10.1007/s12678-021-00674-7.

[47] V.N. Kuleshov, N. V Kuleshov, S.A. Grigoriev, E.Y. Udris, P. Millet, A.S. Grigoriev, Development and characterization of new nickel coatings for application in alkaline water electrolysis, Int. J. Hydrogen Energy. 41 (2016) 36–45. doi:10.1016/j.ijhydene.2015.10.141.

[48] J. Xiao, A.M. Oliveira, L. Wang, Y. Zhao, T. Wang, J. Wang, B.P. Setzler, Y. Yan, Water-Fed Hydroxide Exchange Membrane Electrolyzer Enabled by a Fluoride-Incorporated Nickel-Iron Oxyhydroxide Oxygen Evolution Electrode, ACS Catal. 11 (2021) 264–270. doi:10.1021/acscatal.0c04200.

[49] H. Ito, N. Kawaguchi, S. Someya, T. Munakata, N. Miyazaki, M. Ishida, A. Nakano, Experimental investigation of electrolytic solution for anion exchange membrane water electrolysis, Int. J. Hydrogen Energy. 43 (2018) 17030. doi:10.1016/j.ijhydene.2018.07.143.

[50] H. Ito, N. Miyazaki, S. Sugiyama, M. Ishida, Y. Nakamura, S. Iwasaki, Y. Hasegawa, A. Nakano, Investigations on electrode configurations for anion exchange membrane

electrolysis, J. Appl. Electrochem. 48 (2018) 305–316. doi:10.1007/s10800-018-1159-5.

[51] A.Y. Faid, A.O. Barnett, F. Seland, S. Sunde, Tuning Ni-MoO2Catalyst-Ionomer and Electrolyte Interaction for Water Electrolyzers with Anion Exchange Membranes, ACS Appl. Energy Mater. 4 (2021) 3327. doi:10.1021/acsaem.0c03072.

[52] S. Ghoshal, B.S. Pivovar, S.M. Alia, Evaluating the effect of membrane-ionomer combinations and supporting electrolytes on the performance of cobalt nanoparticle anodes in anion exchange membrane electrolyzers, J. Power Sources. 488 (2021) 229433. doi:10.1016/j.jpowsour.2020.229433.

[53] I. Dedigama, P. Angeli, K. Ayers, J.B. Robinson, P.R. Shearing, D. Tsaoulidis, D.J.L. Brett, In situ diagnostic techniques for characterisation of polymer electrolyte membrane water electrolysers - Flow visualisation and electrochemical impedance spectroscopy, Int. J. Hydrogen Energy. 39 (2014) 4468–4482. doi:10.1016/j.ijhydene.2014.01.026.

[54] S. Siracusano, S. Trocino, N. Briguglio, V. Baglio, A.S. Aric, Electrochemical Impedance Spectroscopy as a Diagnostic Tool in Polymer Electrolyte Membrane Electrolysis, Materials (Basel). 11 (2018) 1368. doi:10.3390/ma11081368.

[55] F. Seland, R. Tunold, D.A. Harrington, Impedance study of methanol oxidation on platinum electrodes, Electrochim. Acta. 51 (2006) 3827. doi:10.1016/j.electacta.2005.10.050.

[56] P. Bevington, Data reduction and error analysis for the physical sciences, in: McGraw-Hill, New York, 1969: p. 200.

[57] F. Jaouen, G. Lindbergh, G. Sundholm, Investigation of Mass-Transport Limitations in the Solid Polymer Fuel Cell Cathode, J. Electrochem. Soc. 149 (2002) A437–A447. doi:10.1149/1.1456916.

[58] F. Jaouen, G. Lindbergh, Transient Techniques for Investigating Mass-Transport Limitations in Gas Diffusion Electrodes, J. Electrochem. Soc. 150 (2003) A1699–A1710. doi:10.1149/1.1624294.

[59] F.D. Speck, K.E. Dettelbach, R.S. Sherbo, D.A. Salvatore, A. Huang, C.P. Berlinguette, On the Electrolytic Stability of Iron-Nickel Oxides, Chem. 2 (2017) 590–597. doi:10.1016/j.chempr.2017.03.006.

[60] J. Chang, Q. Lv, G. Li, J. Ge, C. Liu, W. Xing, Core-shell structured Ni12P5/Ni3(PO4)2 hollow spheres as difunctional and efficient electrocatalysts for overall water electrolysis, Appl. Catal. B Environ. 204 (2017) 486–496. doi:10.1016/j.apcatb.2016.11.050.

[61] C.C. Pavel, F. Cecconi, C. Emiliani, S. Santiccioli, A. Scaffidi, S. Catanorchi, M. Comotti, Highly Efficient Platinum Group Metal Free Based Membrane-Electrode Assembly for Anion Exchange Membrane Water Electrolysis, Angew. Chem. Int. 53 (2014) 1378–1381. doi:10.1002/anie.201308099.

[62] S. Seetharaman, R. Balaji, K. Ramya, K.S. Dhathathreyan, M. Velan, Graphene oxide modified non-noble metal electrode for alkaline anion exchange membrane water electrolyzers, Int. J. Hydrogen Energy. 38 (2013) 14934–14942. doi:10.1016/j.ijhydene.2013.09.033.

[63] L. Xiao, S. Zhang, J. Pan, C. Yang, M. He, L. Zhuang, J. Lu, First implementation of alkaline polymer electrolyte water electrolysis working only with pure water, Energy Environ. Sci. 5 (2012) 7869–7871. doi:10.1039/c2ee22146b.

[64] X. Li, F.C. Walsh, D. Pletcher, Nickel based electrocatalysts for oxygen evolution in high current density, alkaline water electrolysers, Phys. Chem. Chem. Phys. 13 (2011) 1162–1167. doi:10.1039/c0cp00993h.

[65] C.C. Pavel, F. Cecconi, C. Emiliani, S. Santiccioli, A. Scaffidi, S. Catanorchi, M. Comotti, Highly efficient platinum group metal free based membrane-electrode assembly for anion exchange membrane water electrolysis, Angew. Chemie - Int. Ed. 53 (2014) 1378–1381. doi:10.1002/anie.201308099.

[66] D. Chanda, J. Hnát, T. Bystron, M. Paidar, K. Bouzek, Optimization of synthesis of the nickel-cobalt oxide based anode electrocatalyst and of the related membrane-electrode assembly for alkaline water electrolysis, J. Power Sources. 347 (2017) 247–258. doi:10.1016/j.jpowsour.2017.02.057.

[67] B. Motealleh, Z. Liu, R.I. Masel, J.P. Sculley, Z.R. Ni, L. Meroueh, Next-generation anion exchange membrane water electrolyzers operating for commercially relevant lifetimes, Int. J. Hydrogen Energy. 46 (2021) 3379–3386. doi:10.1016/j.ijhydene.2020.10.244.

[68] Y. Zhao, N.M. Vargas-Barbosa, E.A. Hernandez-Pagan, T.E. Mallouk, Anodic deposition of colloidal iridium oxide thin films from hexahydroxyiridate(IV) solutions, Small. 7 (2011) 2087–2093. doi:10.1002/smll.201100485.

[69] J.A. Haber, E. Anzenburg, J. Yano, C. Kisielowski, J.M. Gregoire, Multiphase Nanostructure of a Quinary Metal Oxide Electrocatalyst Reveals a New Direction for OER Electrocatalyst Design, Adv. Energy Mater. 5 (2015) 1402307. doi:10.1002/aenm.201402307.

[70] M. Favaro, W.S. Drisdell, M.A. Marcus, J.M. Gregoire, E.J. Crumlin, J.A. Haber, J. Yano, An Operando Investigation of (Ni-Fe-Co-Ce)Ox System as Highly Efficient Electrocatalyst for Oxygen Evolution Reaction, ACS Catal. 7 (2017) 1248–1258. doi:10.1021/acscatal.6b03126.